Front. Chem. Sci. Eng. 2022, 16(9): 1387–1398
https://doi.org/10.1007/s11705-022-2154-2

RESEARCH ARTICLE

Integrating of metal-organic framework UiO-66-NH_2 and cellulose nanofibers mat for high-performance adsorption of dye rose bengal

Yuyao Han[1,2], **Lei Xia** (✉)[1,2], **Xupin Zhuang**[1,2], **Yuxia Liang**[3]

1 State Key Laboratory of Separation Membranes and Membrane Processes, National Center for International Joint Research on Separation Membranes, Tiangong University, Tianjin 300387, China
2 School of Textile Science and Engineering, Tiangong University, Tianjin 300387, China
3 School of Mathematical Sciences, Tianjin Normal University, Tianjin 300387, China

Abstract UiO-66-NH_2 is an efficient material for removing pollutants from wastewater due to its high specific surface area, high porosity and water stability. However, recycling them from wastewater is difficult. In this study, the cellulose nanofibers mat deacetylated from cellulose acetate nanofibers were used to combine with UiO-66-NH_2 by the method of *in-situ* growth to remove the toxic dye, rose bengal. Compared to previous work, the prepared composite could not only provide ease of separation of UiO-66-NH_2 from the water after adsorption but also demonstrate better adsorption capacity (683 mg·g^{-1} (T = 25 °C, pH = 3)) than that of the simple UiO-66-NH_2 (309.6 mg·g^{-1} (T = 25 °C, pH = 3)). Through the analysis of adsorption kinetics and isotherms, the adsorption for rose bengal is mainly suitable for the pseudo-second-order kinetic model and Freundlich model. Furthermore, the relevant research revealed that the main adsorption mechanism of the composite was electrostatic interaction, hydrogen bonding and π–π interaction. Overall, the approach depicts an efficient model for integrating metal-organic frameworks on cellulose nanofibers to improve metal-organic framework recovery performance with potentially broad applications.

Keywords UiO-66-NH_2, cellulose nanofibers, rose bengal, adsorption, mechanism

1 Introduction

Dyes have been widely used in textiles and other industries in recent years, but they produce a significant amount of colored wastewater [1]. Rose bengal (RB) is a water-soluble pink colour dye used in medical diagnostic applications such as liver function tests, staining of necrotic tissue in the eye, and inactivation of corneal cells in conjunctivitis. RB, despite its numerous clinical applications, poses a serious threat to human health, causing a variety of irritant reactions such as itching, peeling, reddening and even blistering when it comes into contact with the skin or eyes. It also causes mucous membrane damage and respiratory irritation in humans when inhaled. As a result, an effective method of removing RB from wastewater warrants further investigation [2].

Currently, the technologies for the removal of dyes from wastewater can be divided into three categories based on the action mechanism: biological, chemical, and physical [3]. Biological treatment which includes fungal decolorisation, microbial degradation, adsorption by (living or dead) microbial biomass, and bioremediation systems, is one of the most cost-effective methods [4]. Chemical treatment primarily consistent of electroflotation, electrokinetic coagulation, traditional oxidation methods using oxidising agents (ozone), irradiation or electrochemical processes [5]. Membrane-filtration and adsorption methods are the most common physical methods. However, the disadvantage of the membrane-filtration process is the additional cost of replacing the membranes regularly. Adsorption technology has recently received a lot of attention due to its low initial cost, simple and flexible design, insensitivity to toxic pollutants, and lack harmful substance generation [6]. The materials currently used for the adsorption of dye molecules include activated carbon, clay, etc. However, due to the complex diversity of dyes in wastewater, conventional adsorbent materials have their limitations. Some activated carbon, for example, is non-selective and ineffective at dispersing

Received September 23, 2021; accepted December 19, 2021

E-mail: xialei@tiangong.edu.cn

and reducing dyes, whereas natural clays are ineffective at neutral and anionic dyes. As a result, developing a new adsorbent material capable for overcoming the aforementioned issues is a hot topic [7].

Metal-organic frameworks (MOFs), an emerging class of multifunctional porous materials constructed from metal ions or metal clusters and organic ligands through the coordination bonding [8], because of their high surface area, controllably porous structure, and sufficient active adsorption sites, are frequently considered as potential applications for gas storage, sensing, and the removal of dyes or heavy metals [9–11]. Recently, a few attempts have been made to investigate the performance of MOF-based adsorbents for organic dye adsorption removal. For example, Haque et al. [12] fabricated an iron terephthalate (MOF-235), which had been used for the removal of harmful dyes (anionic dye methyl orange and cationic dye methylene blue). In the study of Wang et al. [13], a g-C3N4/ MIL-125(Ti) heterostructures photocatalyst was successfully synthesized, and the obtained composites exhibited more effective photocatalytic properties for the degradation of rhodamine B in aqueous solution under visible light irradiation. In the study of Abdi et al., zeolitic imidazolate framework (ZIF-8) as a MOF and its hybrid nanocomposites based on graphene oxide (GO) and carbon nanotubes (CNTs) were synthesized, the maximum adsorption capacities for malachite green were 1667, 2034 and 3300 $mg \cdot g^{-1}$ for ZIF-8, ZIF-8@CNT and ZIF-8@GO at 20 °C, respectively [14]. However, all too often, wastewater treatment has specific requirements for the form of the adsorbent and easy recycling is more important. Because the MOFs synthesized using the solvothermal methods are nanocrystalline powder particles that must be recycled via filtering or centrifugation, they are clearly unsuitable for using in wastewater treatment.

Nanofibers offer an ideal medium for the incorporation of MOFs into engineered constructs. There are currently three methods for integrating MOFs with nanofibers: 1) 'MOF-first', in which the nanofibers are processed with prefabricated MOFs, the disadvantage of this method is that it disrupts the processing of the fiber precursor solution and may result in deformed fibers; 2) 'combining pre-synthesized MOFs with prefabricated nanofibers using covalent or non-covalent attachment techniques', and the disadvantage of this method is that it usually requires additives, covalent bonding or special methods to bond the MOFs and fibers into a strong composite; 3) 'fiber-first', in which MOFs are *in-situ* grown in or on prefabricated nanofibers as crystals or films. Metal ions or organic ligands in MOFs are thus coordinated to reactive sites on fibers. The method has the advantage of usually preserving the physical properties of the prepared composite and ensuring a uniform coating of MOFs along the fibers [15]. Wang et al. [16] fabricated MOF filters with the composites of PAN and ZIF-67 by the way of *in-situ* growth to remove the organic pollutants in water; In the study of Yang et al. [17], the superhydrophobic cotton fabrics were prepared via *in-situ* growing MiL-125 on the surface of cotton fibers. And Lis et al. [18] directly synthesised HKUST in wool fiber to achieve washing durability and antibacterial properties. These applications and performance enhancements all demonstrate that the *in-situ* growth of MOF on fibers has a lot of potential for removing pollutants from water.

Currently, the electrospinning method is widely used to produce nanofibers, but high voltage, sensitivity to dielectric constant, and low fiber yield limit its wide application. In comparison to electrospinning, centrifugal spinning is a highly efficient, low-cost, and novel method for producing nanofibers [19]. In this method, the solution is ejected under centrifugal force from the spinneret at rapid rotational speeds powered by the motor [20], due to the interaction between turbulent airflow and centrifugal force, and the volatile solvents from the spinning solution evaporate rapidly at the time, and the jet is stretched by uneven forces during its movement. As a result, the solutes have more opportunities to aggregate, and the fibers deposited on the collector have a random arrangement and a larger diameter distribution, allowing for the intertwining of a fluffy mat [21]. All the features can offer more space for the growth of the MOFs crystals of different sizes. And UiO-66-NH_2 is made from zirconium salts that form a $Zr_6O_4(OH)_4$ SBU and 2-aminoterephthalic acid [22]. In this study, we choose UiO-66-NH_2 as an adsorbent, and used *in-situ* generation to anchor UiO-66-NH_2 on the cellulose nanofibers mat (CNFM) that was regenerated from cellulose acetate nanofibers produced by the centrifugal spinning method to form a composite (CNFM@UiO-66-NH_2). The developed composite could not only reach the goal of dye adsorption, but also improve the adsorption efficiency and solve the problem of adsorbent recovery. The structure of RB and UiO-66-NH_2 is shown in Fig. 1.

2 Experimental

2.1 Chemical reagents

Cellulose acetate (CA, 39.8 wt% of acetyl content, Mn = 30000) was purchased from Sigma Aldrich Co., Ltd. (China), and zirconium chloride ($ZrCl_4$, 98%) and 2-aminoterephthalic acid (NH_2-BDC, > 98%) were both purchased from Shanghai Aladdin Chemistry Co., Ltd. (China). Trifluoroacetic acid (99%), *N*,*N*-dimethylformamide (DMF, 99.9%), NaOH, acetone, acetic acid (CH_3COOH, 99%), and ethanol were purchased from Tianjin Fengchuan Chemicals Co., Ltd. (China). All materials were used without further purification.

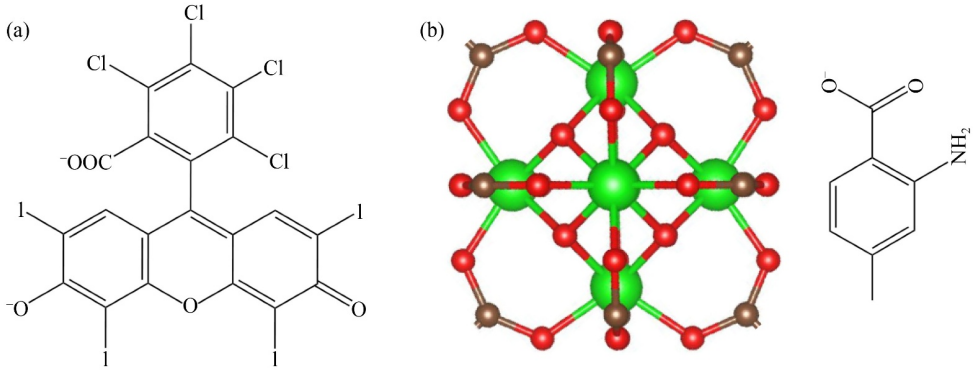

Fig. 1 (a) The structure of RB; (b) $Zr_6O_4(OH)_4$ SBU and 2-aminoterephthalic acid.

2.2 Preparation of CNFM@UiO-66-NH_2

2.2.1 Preparation of CNFM

The centrifugal spinning method was used to make the cellulose nanofiber. To begin, 11% trifluoroacetic acid was used to dissolve the cellulose acetate, and the mixtures were magnetically stirred for 3 h to obtain a homogeneous solution for centrifugal spinning. During the experiment process, the precursor solution in the chamber was ejected from the spinneret under the centrifugal force and the fibers were collected onto the rod collectors by the evaporation of the solvent. The distance between the spinneret and the rod collectors was set as 100 mm. The rotational speed was set to 5500 r·min^{-1} and the inner diameter of the spinneret was 0.16 mm. Acquired cellulose acetate nanofibers were then immersed in 0.05 mol·L^{-1} NaOH solution for 24 h to regenerate CNFM. After that, the mat was washed three times with deionized water for removal of NaOH residues and then dried at 60 °C for 5 h in an oven and stored for further use.

2.2.2 Preparation of UiO-66-NH_2 and CNFM@UiO-66-NH_2

The UiO-66-NH_2 was synthesized through the solvothermal method [23]. Briefly, 2 mmol of $ZrCl_4$, 2 mmol of NH_2-BDC, 32 mL of DMF and 4 mL of CH_3COOH were mixed under ultrasonic treatment for 1 h to get the clear solution and then transferred into a Teflon-lined stainless autoclave. In addition, 0.1 g CNFM was weighted and immersed into the solution at 120 °C for 12 h in an electric oven. The resulting pale-yellow mat was washed with DMF and acetone several times to remove the residues of solvent. The procedure of making the composite mat was shown in Fig. 2. The loading of the UiO-66-NH_2 on the CNFM was determined to be 9.09 wt%

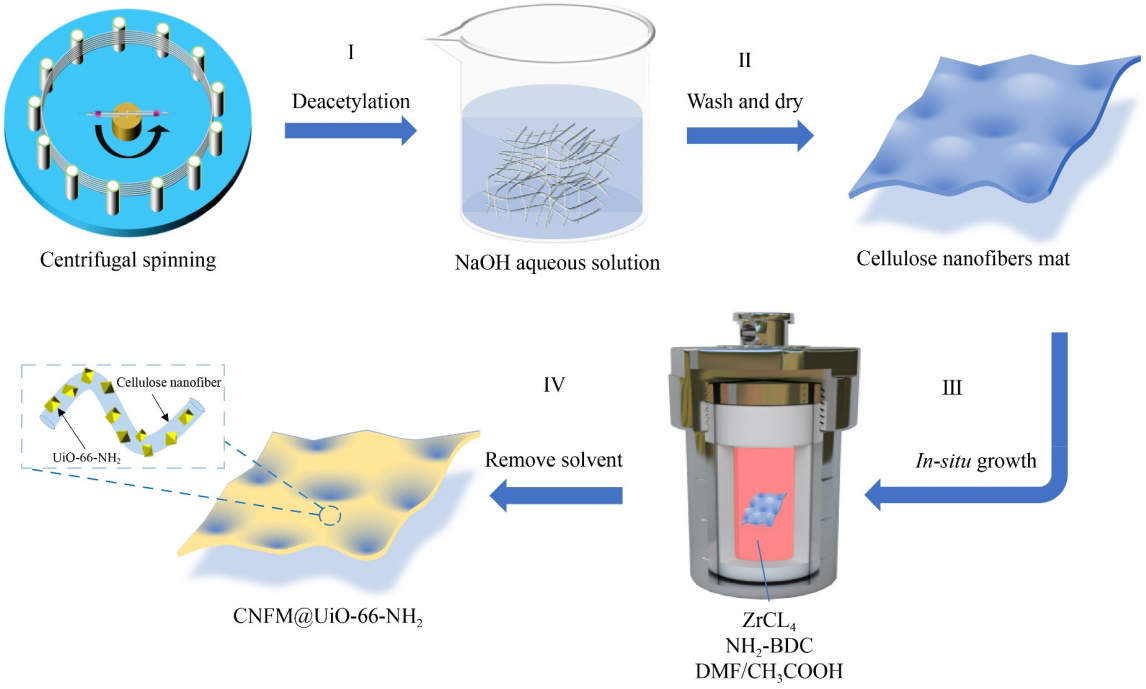

Fig. 2 Fabrication process of CNFM@UiO-66-NH_2.

(approx. 10 mg) based on the weight difference of the CNFM before and after grafting of the MOF. Finally, the CNFM@UiO-66-NH_2 were dried at 60 °C for 5 h in a vacuum oven.

2.3 Characterizations

A Thermal field-emission scanning electron microscope (TFE-SEM; SEM500, Zeiss Co., Germany) equipped with an energy dispersive X-Ray Spectroscopy (EDX) was used to examine the surface morphology and composition. The crystal structure of as-prepared samples was determined using an X-Ray diffractometer (XRD, D8 ADVANCE, BRUKER AXS Co., USA) in the angular range of 2°–50°. Simultaneous thermogravimetric analysis (TGA) and mass spectrometryproperty was used to characterize the thermal properties of the samples (STA449F3, Nietzsche Co., Germany). The infrared absorption spectra were obtained using a Fourier transform infrared spectrometer (FTIR, Nicolet iS50, Thermo Fisher Co., USA). The zeta potential of samples was determined using solid surface zeta potentiometry (SURPASS-3, Anton Paar Co., Austria). X-ray photoelectron spectra (XPS) was used to determine the elemental composition and analysis of samples (K-alpha, Thermo Fisher Co., USA).

2.4 Adsorption experiments

The adsorption experiments were performed on a thermostatic temperature shaker at the speed of 190 r·min^{-1}, and the effects of contact time, initial pH, and the concentration of dyes were investigated. As-prepared CNFM@UiO-66-NH_2 and 10 mg UiO-66-NH_2 were dispersed into 50 mL RB solution with designated experimental values, respectively (concentration of RB was 50 mg·L^{-1}, pH = 3, T = 25 °C). The concentration of RB in the solution was determined using a UV-Vis spectrophotometer at a wavelength of 545 nm and the adsorption capacity and removal efficiency were calculated using the equation below:

$$q_t = \frac{(C_0 - C_t) \times V}{M}, \tag{1}$$

$$\text{The remove efficiency } (\%) = \frac{C_0 - C_t}{C_0} \times 100\%, \tag{2}$$

where q_t (mg·g^{-1}) is adsorbed amount at time t, C_0 (mg·L^{-1}) and C_t (mg·L^{-1}) are concentrations of RB in the solution at initial and time t, V is the liquid phase volume (mL), and M is the mass of the absorbent.

2.5 Adsorption kinetic and isotherm studies

The adsorption kinetics were explored at 25 °C to investigate the adsorption rate of CNFM@UiO-66-NH_2 for RB, and the data were fit by the pseudo-first-order (PFO) and pseudo-second-order (PSO) kinetic model. The equations were as follows:

$$\ln (q_e - q_t) = \ln q_e - k_1 t, \tag{3}$$

$$\frac{t}{q_t} = \frac{1}{k_2 \cdot q_e^2} + \frac{t}{q_e}, \tag{4}$$

where k_1 and k_2 are the constants of first-order kinetic constant and second-order kinetic, respectively, and q_e (mg·g^{-1}) is the equilibrium adsorption capacity. To further valuate the adsorption capacity of CNFM@UiO-66-NH_2 for the RB, two classical isotherms, i.e., Langmuir and Freundlich's models, were used to simulate the adsorption process. The equations used for analysing data were as follows:

$$\frac{C}{q_e} = \frac{C}{q_{max}} + \frac{1}{q_{max} \cdot K_L}, \tag{5}$$

$$\ln q_e = \ln K_F + \frac{1}{n} \cdot \ln C, \tag{6}$$

where K_F and K_L are Freundlich constant and Langmuir constant, respectively, $1/n$ is Freundlich constant related to the adsorption, and q_{max} (mg·g^{-1}) is maximum adsorption capacity.

3 Results and discussion

3.1 Characterization of CNFM@UiO-66-NH_2

The morphology of the cellulose acetate nanofibers prepared by centrifugal spinning was shown in Fig. 3. It could be seen that the nanofiber mass is similar to a tuft of cotton. Because of the interaction between turbulent airflow and centrifugal force, the jet ejected from the spinneret is unstable, the volatile solvents evaporate quickly, the solutes can aggregate, resulting in a random arrangement between nanofibers (Fig. 3(b)) and broad distribution in fiber diameters (Fig. 3(c)). To regenerate cellulose nanofibers, the as-prepared cellulose acetate nanofibers were immersed in NaOH solution for deacetylation. The cellulose nanofibers regenerated after deacetylation was washed and dried to form a fluffy and lightweight, and its morphology was shown in Fig. 3(d). It is essential to investigate whether the process of deacetylation changes the morphology of nanofibers. As shown in Figs. 3(e) and 3(f), the regenerated cellulose nanofibers retained their random arrangement and broad fiber diameter distribution, and the main difference was that the overall diameter of the cellulose nanofibers was reduced. When combined with UiO-66-NH_2, the CNFM turned pale yellow but still retained its fluffy and light character without losing physical properties, as shown in Fig. 3(g). The SEM image of CNFM@UiO-66-NH_2 was

shown in Fig. 3(h), demonstrating that the UiO-66-NH_2 were regular octahedrons, and the growth of crystallites formed a continuous and homogeneous coating on the nanofibers. Not only that, the elements C, O, N, Zr were detected in CNFM@UiO-66-NH_2 by EDX mapping, and it could further affirm that UiO-66-NH_2 had successfully grown on the surface of CNFM (Fig. 3(i)).

The result of successful deacetylation and *in-situ* growth of UiO-66-NH_2 was proved by the FTIR absorbance spectra which is shown in Fig. 4. The FTIR spectrum for neat cellulose acetate nanofibers showed the characteristic peaks of cellulose acetate attributed to the vibration of acetate group C–O at 1741 and C–O–C and 1228 cm^{-1}, which these peaks disappeared after deacetylation, as shown in the spectrum. Furthermore, the crucial absorption peak appeared in the spectrum of deacetylated cellulose acetate nanofibers at 3400 cm^{-1} which was attributed to O–H groups [24]. The disappearance of cellulose acetate peaks and the appearance of O–H peak in the deacetylated cellulose acetate nanofibers indicated that the cellulosic structure had been regenerated from cellulose acetate. As shown in Fig. 4(b), the characteristic peaks of cellulose structure at around 1000–1200 cm^{-1} were detected in the CNFM@UiO-66-NH_2. Moreover, the four characteristic peaks of UiO-66-NH_2 were also observed in the composite. The absorption bands at 1574 and 1430 cm^{-1}, which assign to the Zr-bound vibration and C=C from aromatic, respectively [25], and the adsorption bands at 1258 and 764 cm^{-1} are C–N stretching band and N–H wagging band, respectively [26]. The appearance of these peaks in the CNFM@UiO-66-NH_2 demonstrates that the UiO-66-NH_2 had been loaded on the cellulose nanofibers. Further evidence of successful growth of the UiO-66-NH_2 on cellulose nanofibers can be obtained from XRD spectra (Fig. 4(c)). The XRD data of CNFM@UiO-66-NH_2 and UiO-66-NH_2 showed great agreement at 7.4° and 8.5°, which were the characteristic peaks of UiO-66-NH_2 [27]. Furthermore, the load capacity of UiO-66-NH_2 on the CNFM was assessed. Due to the fluffy nature of cellulose acetate nanofibers produced by the centrifugal spinning method, the thickness of deacetylated CNFM is uneven. As a result, it is impossible to ensure that the volume and density of each piece of fiber are comparable, making the quality of each piece of fiber the most convenient parameter to control in comparison. As shown in Fig. 4(d), as

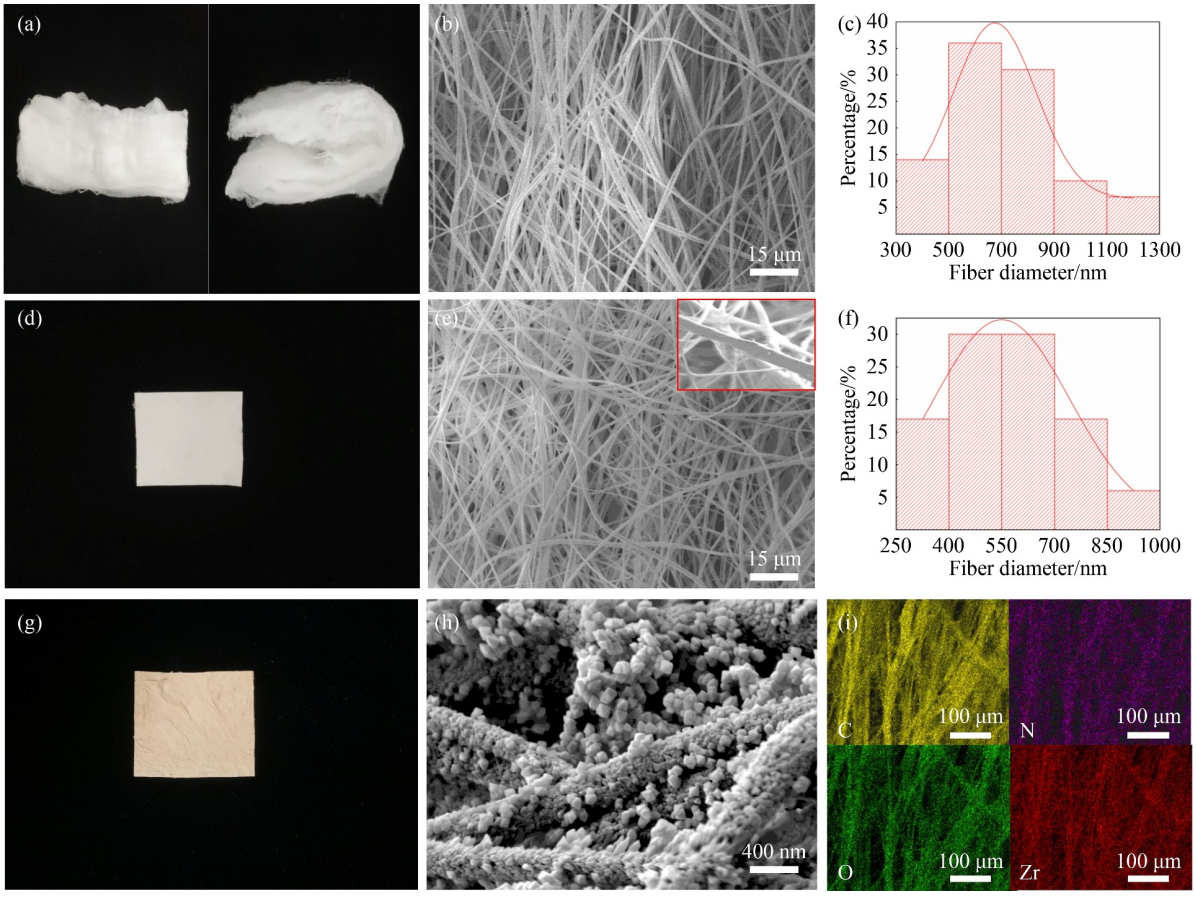

Fig. 3 (a) Cellulose acetate nanofibers produced by centrifugal spinning; (b) SEM image of cellulose acetate nanofibers and (c) its diameter distribution; (d) CNFM; (e) SEM image of CNFM and the surface of nanofiber (insert); (f) diameter distribution of cellulose nanofibers; (g) CNFM@UiO-66-NH_2; (h) SEM image of CNFM@UiO-66-NH_2; (i) EDX elemental mapping of CNFM@UiO-66-NH_2.

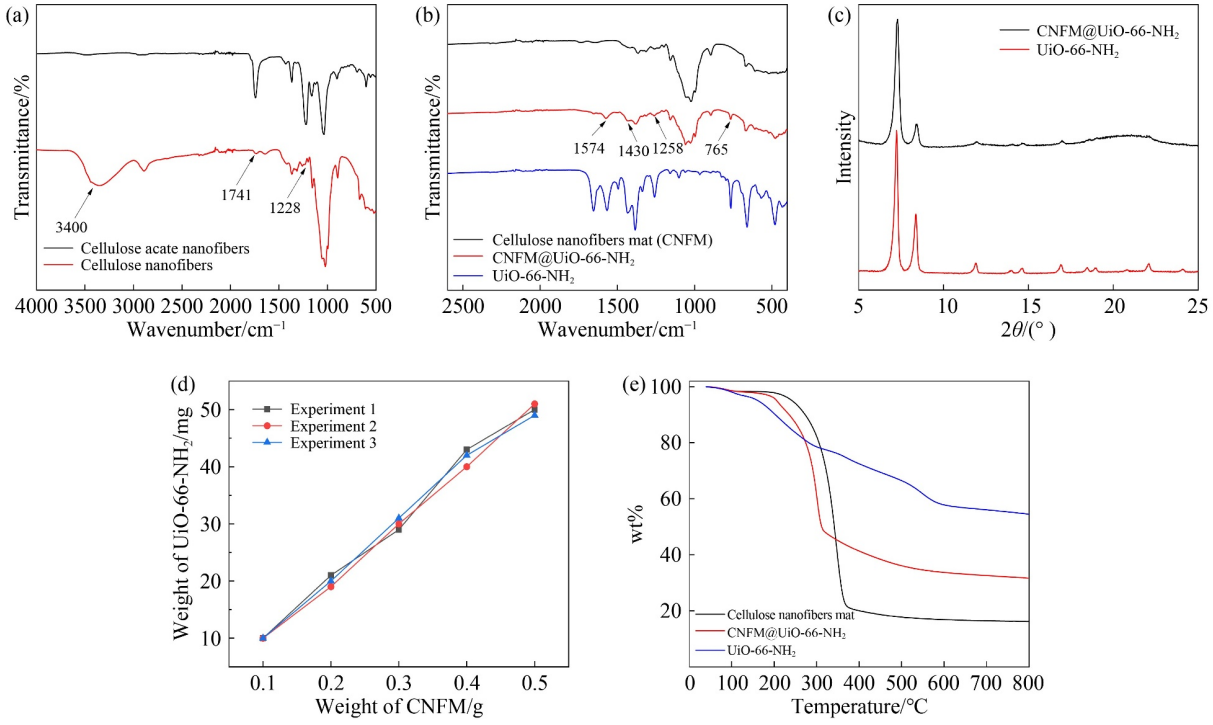

Fig. 4 (a) FTIR spectra of cellulose acetate nanofiber and cellulose nanofiber; (b) FTIR spectra of CNFM, CNFM@UiO-66-NH_2, and UiO-66-NH_2; (c) XRD patterns of CNFM@UiO-66-NH_2 and UiO-66-NH_2; (d) the growth trend of UiO-66-NH_2 on the CNFM of different weight; (e) TGA analyses of CNFM, CNFM@UiO-66-NH_2, and UiO-66-NH_2.

the weight of CNFM increases, so does the fiber count, and the loading capacity of UiO-66-NH_2 on CNFM is then enhanced. In summary, at the same experiment condition, the trend of the growth of MOF crystallites is that each of 0.1 g CNFM can load approximately 10 mg of UiO-66-NH_2.

The TGA reveals that the thermal stability of CNFM@UiO-66-NH_2 can be obtained by combining the properties of CNFM and UiO-66-NH_2 (Fig. 4(e)). The first mass loss in the range of temperature from 40 to 200 °C was due to the evaporation of adsorbed water vapor in the pore channels and incompletely treated solvent molecules, and the CNFM@UiO-66-NH_2 and CNFM had the same characteristics at this temperature range. The second mass loss was caused by the pyrolysis of the functional groups at temperatures ranging from 200 to 420 °C. The mass loss around 420 °C was caused by the decomposition of the UiO-66-NH_2, and at this temperature range, the CNFM@UiO-66-NH_2 also showed features of UiO-66-NH_2.

The Brunner–Emmett–Teller (BET) surface areas were calculated using N_2 adsorption–desorption isotherm, the results were shown in Fig. 5. The BET surface areas of UiO-66-NH_2 and CNFM@UiO-66-NH_2 were 912 $m^2 \cdot g^{-1}$ and 139 $m^2 \cdot g^{-1}$, respectively. The reduction of the BET surface area can be attributed to the growth of UiO-66-NH_2 on the surface of the cellulose nanofiber mat. Similarly, when compared with CNFM@UiO-66-NH_2, the BET surface area of CNFM@UiO-66-NH_2 loaded RB was further reduced from 139 $m^2 \cdot g^{-1}$ to 72 $m^2 \cdot g^{-1}$, which can be attributed to the introduction of RB molecules. The pore size distribution of CNFM@UiO-66-NH_2 was displayed in Fig. 5(b), and the peak at 14.034 Å is from the micropore structure of CNFM@UiO-66-NH_2. The larger size of the pores of the adsorbent relative to the size of the RB molecules suggests that the adsorption process can occur within the pores of the adsorbent.

3.2 Adsorption kinetics

The adsorption kinetics of CNFM@UiO-66-NH_2 and UiO-66-NH_2 was investigated by studying the adsorption of RB at different contact times, and the obtained data were presented in Fig. 6. In a nutshell, the adsorption processes of CNFM@UiO-66-NH_2 could be completed within 30 min, and the UiO-66-NH_2 could be essentially completed within 50 min, and then all the samples reached maximum adsorption at a slowly increasing rate. The situation was because the adsorption sites provided on the adsorbent surface of composite fibers were gradually occupied by RB and saturated, with spatial barriers preventing further contact of RB with the functional groups on the adsorbent surface. As shown in Fig. 6(a), while the initial concentration was 50 $mg \cdot L^{-1}$, the maximum adsorption capacities of CNFM@UiO-66-NH_2 and UiO-66-NH_2 for RB reached 234.2 and 145.3 $mg \cdot g^{-1}$, respectively. It is worth mentioning that, the presence of a large number of hydroxyl groups on the surface of cellulose makes the adsorption capacity of CNFM for anionic dyes very weak. Because the concentration of RB solution after

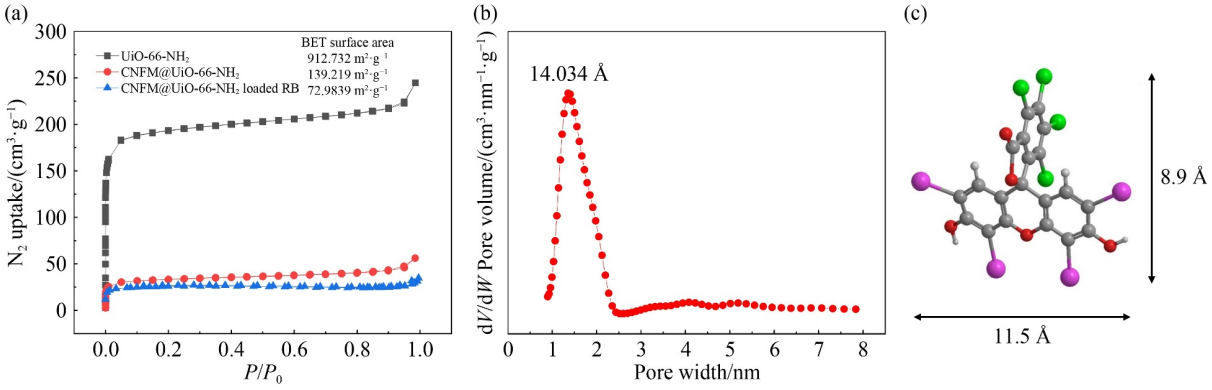

Fig. 5 (a) N_2 adsorption–desorption isotherms of UiO-66-NH_2, CNFM@UiO-66-NH_2, CNFM@UiO-66-NH_2 loaded RB; (b) pore size distribution of CNFM@UiO-66-NH_2; (c) the size of RB molecule.

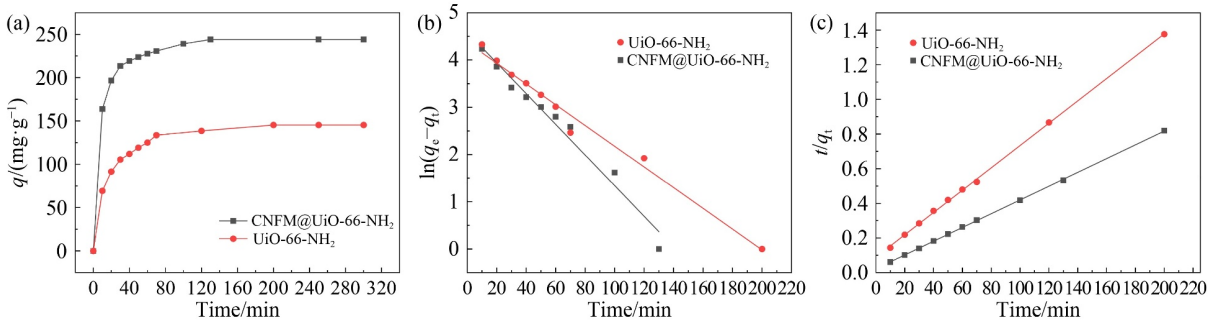

Fig. 6 (a) Effect of contact time on RB adsorption of CNFM@UiO-66-NH_2 and UiO-66-NH_2 (initial concentration = 50 mg·L^{-1}, pH = 3, T = 25 °C); (b) PFO and (c) PSO for the adsorption of RB by CNFM@UiO-66-NH_2 and UiO-66-NH_2.

adsorption CNFM did not change significantly when measured with a UV spectrometer, we simply considered CNFM to be a platform for immobilising MOF crystals. The tested results indicated that loading UiO-66-NH_2 onto CNFM not only solved the problem of difficult collection of UiO-66-NH_2 powder, but also reduced the agglomeration of MOF crystals and expanded the distribution of adsorption sites [28], allowing the MOF crystals on the CNFM@UiO-66-NH_2 to have more access to RB, and thus increasing the adsorption capacity.

The theoretical analysis and the review of the literature revealed that the PFO represented the conditions of 1) at high initial concentrations of adsorbate; 2) at the initial stage of adsorption, and 3) few active sites exist in the adsorbent material. In some cases, the PFO model can be used to describe the diffusional kinetics process. The PSO model could represent the following conditions of 1) at low initial concentrations of adsorbate; 2) at the final stage of adsorption, and 3) the adsorbent is abundant with active sites [29]. In general, the PFO model is suitable for describing adsorption mechanisms associated with physical adsorption and diffusion [30]. While the PSO model is designed for chemisorption processes [31]. To further analyze the adsorption kinetics data, the two models were used to fit the kinetics experimental data for the composite fibers. The processed data were shown in Table 1. The results exhibited that the correlation coefficients (R^2) values of lines of CNFM@UiO-66-NH_2 and UiO-66-NH_2 fitted by the PSO were all higher than 0.99 when compared to the values fitted by the PFO model. Furthermore, the adsorption capacity values calculated by the PSO model were closer to the experimental real values. These findings suggested that chemisorption was the primary determinant of RB adsorption performance.

3.3 Adsorption isotherms

Temperature is an important parameter that has a significant influence on the RB adsorption of CNFM@UiO-66-NH_2 and UiO-66-NH_2. The isotherms experiments were explored under three different temperatures but the same pH value (pH = 3), and the results were exhibited in Fig. 7. It could be seen that with the increase of temperature, the adsorption capacities of CNFM@UiO-66-NH_2 and UiO-66-NH_2 were both increased, suggesting that the adsorption of RB onto the aforementioned absorbent was a spontaneous endothermic process. Furthermore, the CNFM@UiO-66NH_2 had a higher removal efficiency for RB than that of the UiO-66-NH_2. When the initial concentration was 50 mg·L^{-1}, the removal efficiency of CNFM@UiO-66-NH_2 could reach 94% at 25 °C, while that of UiO-66-NH_2 was only 58% under the same conditions. The maximum equilibrium adsorption capacities of CNFM@

Table 1 Kinetic parameters for RB adsorption by CNFM@UiO-66-NH_2 and UiO-66-NH_2

Sample	C_0/(mg·L^{-1})	$q_{e,exp}$/(mg·g^{-1})	PFO kinetic model			PSO kinetic model		
			$q_{e,cal}$/(mg·g^{-1})	k_1	R^2	$q_{e,cal}$/(mg·g^{-1})	k_2	R^2
CNFM@UiO-66-NH_2	50	244.03	174.95	0.0325	0.968	253.56	0.000741	0.999
UiO-66-NH_2	50	145.325	243.67	0.02196	0.983	154.15	0.000528	0.999

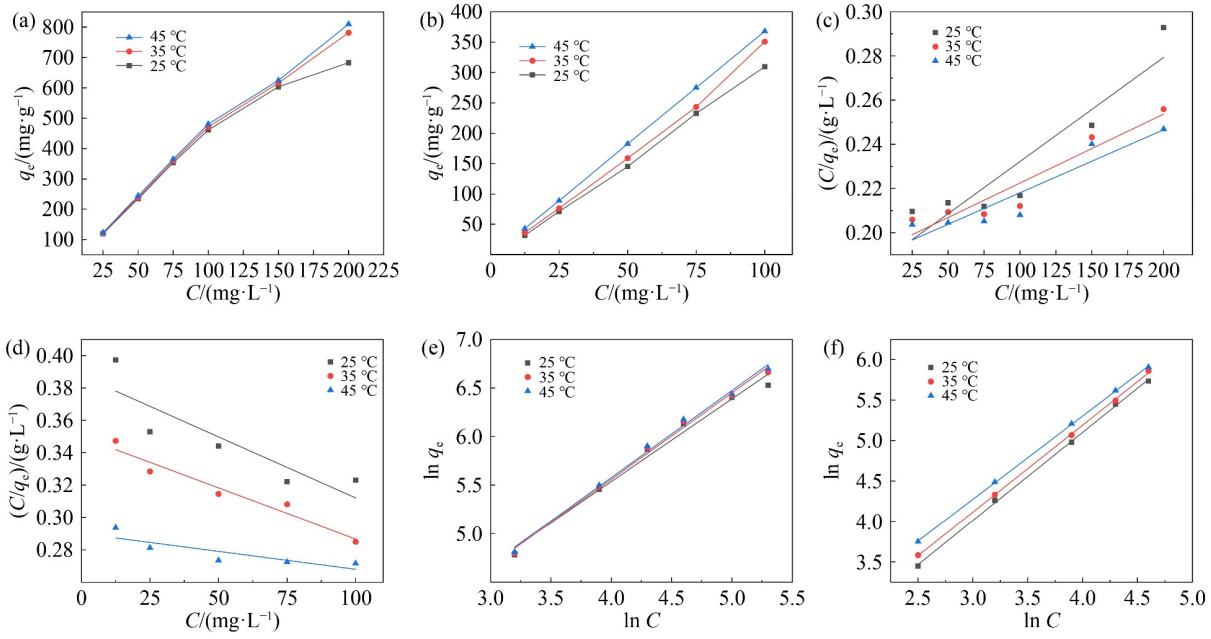

Fig. 7 Equilibrium isotherms for RB adsorption of (a) CNFM@UiO-66-NH_2 and (b) UiO-66-NH_2; Langmuir isotherm model of (c) CNFM@UiO-66-NH_2 and (d) UiO-66-NH_2; Freundlich isotherm model of (e) CNFM@UiO-66-NH_2 and (f) UiO-66-NH_2.

UiO-66-NH_2 were 683, 781.6, and 809.9 mg·g^{-1}, at 25, 35, 45 °C, respectively. But those of UiO-66-NH_2 were 309.6, 350.8, 368 mg·g^{-1}, at 25, 35, 45 °C, respectively. These results indicated that the prepared CNFM@UiO-66-NH_2 could be a very promising adsorbent for RB.

To investigate the adsorption behavior in greater depth, the isotherm data was analyzed using the Langmuir and Freundlich models. Table 2 displays the processed data. In general, the Langmuir isotherm is based on the following assumptions: 1) monolayer adsorption; 2) homogeneous distribution of adsorption sites; 3) constant adsorption energy; and 4) negligible interaction between adsorbate molecules [32]. The Freundlich model is used to describe multi-layer adsorption on heterogeneous surfaces [33]. When the correlation coefficients were compared, the Freundlich model was found to be more appropriate for describing the adsorption process. Meanwhile, the calculated values matched the experimental values more clearly. From the above results, the adsorption of RB onto the CNFM@UiO-66-NH_2 could be considered as a chemisorption process taking place on multiple levels.

3.4 Adsorption mechanism

Because the pH of dye solution is a critical parameter that can affect the adsorption capacity by influencing the protonation/deprotonation of –NH_2 on the surface of

Table 2 Langmuir and Freundlich isotherm parameters for RB adsorption by CNFM@UiO-66-NH_2 and UiO-66-NH_2

Sample	T/°C	Langmuir model			Freundlich model		
		q_m/(mg·g^{-1})	K_L	R^2	K_F	n	R^2
CNFM@UiO-66-NH_2	25	683	0.0079	0.83	8.42	1.175	0.98
	35	781.6	0.0067	0.87	7.41	1.125	0.99
	45	809.9	0.0065	0.85	7.34	1.116	0.99
UiO-66-NH_2	25	309.6	2.581	0.7	2.1	0.918	0.99
	35	350.8	2.859	0.93	2.43	0.93	0.99
	45	368	3.447	0.63	3.27	0.971	0.99

UiO-66-NH_2, some experiments were conducted in the pH range of 3 to 9 to investigate the effect of pH on the adsorption capacity of CNFM@UiO-66-NH_2 for RB. As shown in Fig. 8, the adsorption capacity decreased with the increase of pH value, and at pH 6 there was a significant decrease in the equilibrium adsorption capacity when compared to the previous pH values. To investigate the behaviors, the zeta potentials of CNFM@UiO-66-NH_2 at different pH values were investigated. As shown in Fig. 8(b), when the pH value was less than 5, the surface potential of CNFM@UiO-66-NH_2 was positive and the adsorption capacity of the anionic RB was enhanced due to electrostatic attraction. With a further increase in pH, there is no protonation of amino groups resulting in a negative charge on the surface of CNFM@UiO-66-NH_2. The result of the experiment would explain why the adsorption capacity of RB is reduced at pH 6.

The XPS high-solution spectra before and after adsorption were performed. As shown in Fig. 8(c), a peak of Cl 2p was detected after the adsorption of the composite fibers, it is worth mentioning that the adsorption process was performed in CH_3COOH solution rather than in HCL solution, so the result indicated that the RB was adsorbed by CNFM@UiO-66-NH_2. To gain insight into the mechanisms of RB adsorption onto CNFM@UiO-66-NH_2, the XPS high-resolution spectra were analyzed (Fig. 9). As shown in Fig. 9(a), the deconvoluted Zr 3d spectra consisted of two main peaks at 184.9 eV which could be assigned to Zr–O and 182.6 eV which could be assigned to Zr–OH or –COO–Zr, respectively [34]. After the adsorption of RB, the 184.9 eV peak and 182.6 eV peak all receded significantly by 0.1 eV. The defective UiO-66-NH_2 was investigated using TGA data (Fig. 8(d)), and it was discovered that the molar ratio between Zr and organic linkers was greater than 1, indicating the presence of defects in the UiO-66-NH_2. Previous research work has shown that coordinating the cationic Zr site to an anionic functional group, result in a significant shift in the XPS spectra of Zr 3d [35]. As a result, we conclude in this paper that the cationic Zr site ligates with the negatively charged dye solely through electrostatic forces rather than coordination. Furthermore, as shown in Fig. 9(c), one main peak at 399.3 eV in the high-resolution N 1s spectra could be assigned to N in the phenylamine group [36]. Similarly, after the adsorption of RB for the composite fibers, the position of the peak shifted back, suggesting that $–NH_2$ played a key role in the adsorption process. The effect of π–π interaction between RB and CNFM@UiO-66-NH_2 was explored by XPS C 1s (Fig. 9(b)). Four peaks were observed in the deconvoluted C 1s spectra which were 284.5 (C1), 285.6 (C2), 286.5 (C3), 288.5 eV (C4), respectively. The C1 was assigned to

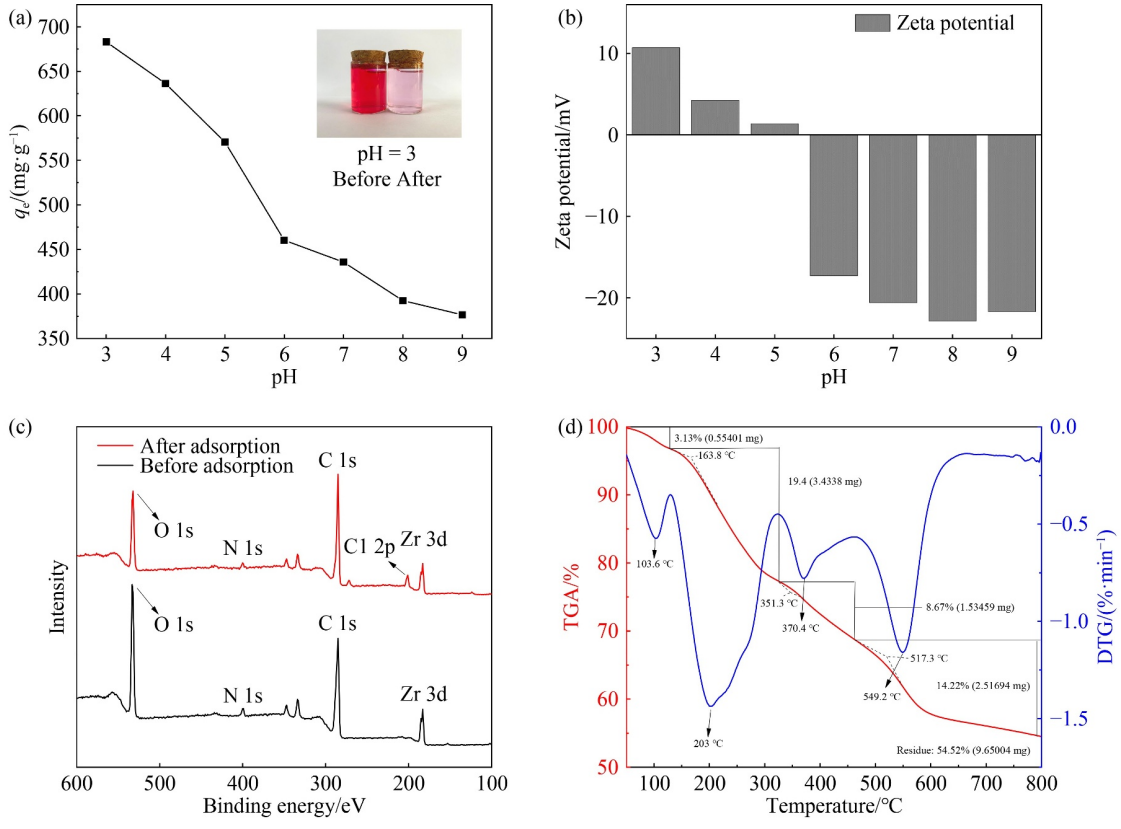

Fig. 8 (a) Effect of pH on RB adsorption of CNFM@UiO-66-NH_2 (initial concentration = 200 mg·L^{-1}, T = 25 °C, contact time = 300 min); (b) Zeta potentials of CNFM@UiO-66-NH_2 at varied pH values; (c) XPS spectra of CNFM@UiO-66-NH_2 before and after adsorption; (d) TGA and DTG curves of UiO-66-NH_2.

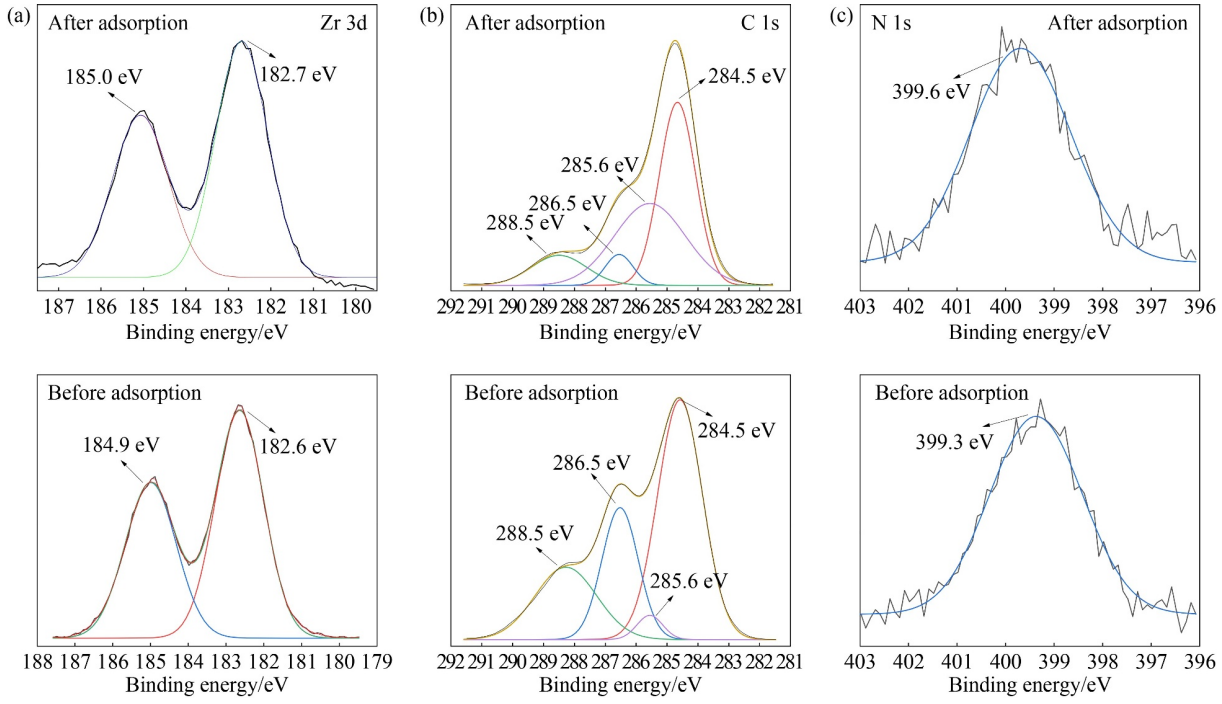

Fig. 9 XPS high-resolution spectra of (a) Zr 3d, (b) C 1s, (c) N 1s for CNFM@UiO-66-NH_2 before and after adsorption.

extensively delocalized sp^2 bonds of benzene, C2 was ascribed to localized sp^2 bonds of benzene, C3 was assigned to $-CH_2-C=O$ and the C4 was corresponded to −COO− [34]. The TS asymmetry index of the Dexter spectral line shape was represented by the C2/C1 intensity ratio, and the TS asymmetry index value of RB-loaded CNFM@UiO-66-NH_2 was 0.4, while the pristine CNFM@UiO-66-NH_2 was 0.1, confirming the strong influence of π–π interactions on the adsorption of RB [37].

3.5 Influence of co-existing ions

Real wastewater frequently contains co-existing cations and anions in addition to dye. As a result, to evaluate the potential of CNFM@UiO-66-NH_2 in real water, further research into its adsorption performance is required. In this work, several common inorganic salts including NaCl, $NaNO_3$, Na_2SO_4, were selected. As shown in Fig. 10, these co-existing salts have negligible effect on RB adsorption, indicating that CNFM@UiO-66-NH_2 may be a suitable adsorbent for RB in real wastewater.

3.6 Reusability of CNFM@UiO-66-NH_2

The CNFM@UiO-66-NH_2 was regenerated by washing with ultrasound for 10 min in 100 mL ethanol solution, and the procedure was performed three times. The regenerated sample was then used for adsorption once again. After six consecutive cycles, the adsorption capacity of CNFM@UiO-66-NH_2 remained at 86% of the maximum adsorption capacity (Fig. 10(b)). The obtained result indicated that the MOF crystal structure on cellulose was still intact. Furthermore, a comparison of the adsorption capacity of CNFM@UiO-66-NH_2 and other adsorbent materials for RB is shown in Fig. 10(c), and it can be

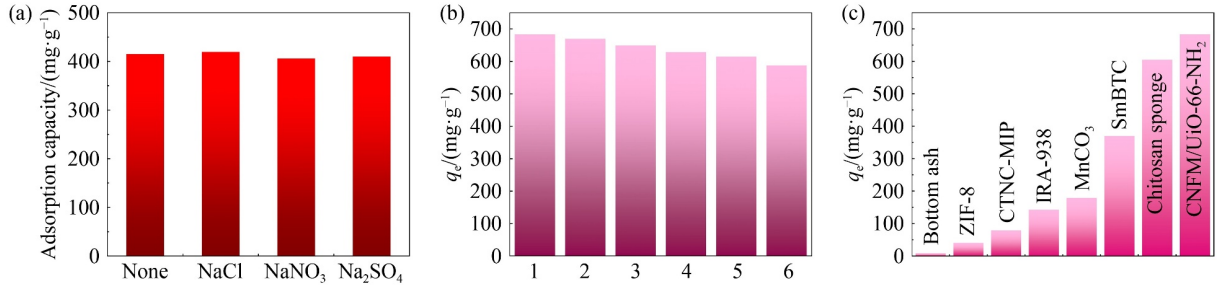

Fig. 10 (a) Adsorption capacities of CNFM@UiO-66-NH_2 cycle number in the RB solutions containing other common inorganic salts (T = 25 °C, pH = 7, and the molar concentrations of these salts are consistent with that of RB); (b) the adsorption capacity of CNFM@UiO-66-NH_2 after different cycle numbers; (c) the adsorption capacity of CNFM@UiO-66-NH_2 and other materials [1,2,38–42].

seen that CNFM@UiO-66-NH_2 has a superior adsorption capacity. This illustrates that the prepared sample is very promising for the adsorption of RB.

4 Conclusions

In this study, we developed and prepared a composite material using the *in-situ* generation to grow UiO-66-NH_2 uniformly on the cellulose nanofibers surface for the adsorption of the RB. When the initial concentration was 50 mg·L^{-1}, the removal efficiency of CNFM@UiO-66-NH_2 could reach 94% at 25 °C, while that of UiO-66-NH_2 was only 58% under the same conditions, and the adsorption process of CNFM@UiO-66-NH_2 is approximately 20 min faster than that of UiO-66-NH_2. The maximum adsorption capacity of CNFM@UiO-66-NH_2 in the experiment was 683 mg·g^{-1} (pH = 3, T = 25 °C), but that of UiO-66-NH_2 was 309.6 mg·g^{-1} (pH = 3, T = 25 °C). By the analysis of specific adsorption experiments, the adsorption behavior of RB followed the PSO model and the Freundlich model, indicating that the adsorption process was chemisorption occurring on a multi-layer with an inhomogeneous surface. According to zeta potential analysis and XPS studies, the main adsorption mechanisms were electrostatic interaction, hydrogen bonding, and π–π interaction. Furthermore, the prepared composite material can address the issue of UiO-66-NH_2 powder being difficult to recover or remove from the solution. Even after six adsorption–desorption cycles, it retained at 86% of its optimum adsorption capacity, demonstrating the composite material's high reusability. Finally, the current study provided some novel ideas and approaches for treating wastewater containing various dyes.

Acknowledgments The authors gratefully acknowledge the financial support of the Tianjin Natural Science Foundation (Grant No. 18JCQNJC71900).

References

1. Lee L W, Pao S Y, Pathak A, Kang D Y, Lu K L. Membrane adsorber containing a new Sm(III)-organic framework for dye removal. Environmental Science: Nano, 2019, 6(4): 1067–1076
2. Gupta V K, Mittal A, Jhare D, Mittal J. Batch and bulk removal of hazardous colouring agent rose bengal by adsorption techniques using bottom ash as adsorbent. RSC Advances, 2012, 2(22): 8381–8389
3. Crini G. Non-conventional low-cost adsorbents for dye removal: a review. Bioresource Technology, 2006, 97(9): 1061–1085
4. McMullan G, Meehan C, Conneely A, Kirby N, Robinson T, Nigam P, Banat I M, Marchant R, Smyth W E. Microbial decolourisation and degradation of textile dyes. Applied Microbiology and Biotechnology, 2001, 56(1-2): 81–87
5. Fu F L, Wang Q. Removal of heavy metal ions from wastewaters: a review. Journal of Environmental Management, 2011, 92(3): 407–418
6. Dabrowski A. Adsorption—from theory to practice. Advances in Colloid and Interface Science, 2001, 93(1-3): 135–224
7. Rafatullah M, Sulaiman O, Hashim R, Ahmad A. Adsorption of methylene blue on low-cost adsorbents: a review. Journal of Hazardous Materials, 2010, 177(1-3): 70–80
8. Kumar P, Pournara A, Kim K H, Bansal V, Rapti S, Manos M J. Metal-organic frameworks: challenges and opportunities for ion-exchange/sorption applications. Progress in Materials Science, 2017, 86: 25–74
9. Schoenecker P M, Carson C G, Jasuja H, Flemming C J J, Walton K S. Effect of water adsorption on retention of structure and surface area of metal-organic frameworks. Industrial & Engineering Chemistry Research, 2012, 51(18): 6513–6519
10. Yazaydin A O, Benin A I, Faheem S A, Jakubczak P, Low J J, Willis R R, Snurr R Q. Enhanced CO_2 adsorption in metal-organic frameworks via occupation of open-metal sites by coordinated water molecules. Chemistry of Materials, 2009, 21(8): 1425–1430
11. Kumar P, Deep A, Kim K H. Metal organic frameworks for sensing applications. Trends in Analytical Chemistry, 2015, 73: 39–53
12. Haque E, Lo V, Minett A I, Harris A T, Church T L. Dichotomous adsorption behaviour of dyes on an amino-functionalised metal-organic framework, amino-MIL-101(Al). Journal of Materials Chemistry A, 2014, 2(1): 193–203
13. Wang H, Yuan X Z, Wu Y, Zeng G M, Chen X H, Leng L J, Li H. Synthesis and applications of novel graphitic carbon nitride/metal-organic frameworks mesoporous photocatalyst for dyes removal. Applied Catalysis B: Environmental, 2015, 174: 445–454
14. Abdi J, Vossoughi M, Mahmoodi N M, Alemzadeh I. Synthesis of metal-organic framework hybrid nanocomposites based on GO and CNT with high adsorption capacity for dye removal. Chemical Engineering Journal, 2017, 326: 1145–1158
15. Peterson G W, Lee D T, Barton H F, Epps T H III, Parsons G N. Fibre-based composites from the integration of metal-organic frameworks and polymers. Nature Reviews Materials, 2021, 6(7): 605–621
16. Wang C H, Cheng P, Yao Y Y, Yamauchi Y, Yan X, Li J S, Na J. *In-situ* fabrication of nanoarchitectured MOF filter for water purification. Journal of Hazardous Materials, 2020, 392: 122164
17. Yang Y Y, Huang W, Guo Z P, Zhang S Y, Wu F, Huang J J, Yang H J, Zhou Y S, Xu W L, Gu S J. Robust fluorine-free colorful superhydrophobic PDMS/NH_2-MIL-125(Ti)@cotton fabrics for improved ultraviolet resistance and efficient oil-water separation. Cellulose, 2019, 26(17): 9335–9348
18. Lis M J, Caruzi B B, Gil G A, Samulewski R B, Bail A, Scacchetti F A P, Moises M P, Bezerra F M. *In-situ* direct synthesis of HKUST-1 in wool fabric for the improvement of antibacterial properties. Polymers, 2019, 11(4): 713
19. Xia L, Ju J G, Xu W, Ding C K, Cheng B W. Preparation and characterization of hollow Fe_2O_3 ultra-fine fibers by centrifugal spinning. Materials & Design, 2016, 96: 439–445
20. Ren L Y, Ozisik R, Kotha S P, Underhill P T. Highly efficient fabrication of polymer nanofiber assembly by centrifugal jet

spinning: process and characterization. Macromolecules, 2015, 48(8): 2593–2602

21. Hu M R, Wang Y F, Yan Z F, Zhao G D, Zhao Y X, Xia L, Cheng B W, Di Y B, Zhuang X P. Hierarchical dual-nanonet of polymer nanofibers and supramolecular nanofibrils for air filtration with a high filtration efficiency, low air resistance and high moisture permeation. Journal of Materials Chemistry A, 2021, 9(24): 14093–14100
22. Ru J, Wang X M, Wang F B, Cui X L, Du X Z, Lu X Q. UiO series of metal-organic frameworks composites as advanced sorbents for the removal of heavy metal ions: synthesis, applications and adsorption mechanism. Ecotoxicology and Environmental Safety, 2021, 208: 111577
23. Butova V V, Soldatov M A, Guda A A, Lomachenko K A, Lamberti C. Metal-organic frameworks: structure, properties, methods of synthesis and characterization. Russian Chemical Reviews, 2016, 85(3): 280–307
24. Kalwar K, Hu L, Li D L, Shan D. AgNPs incorporated on deacetylated electrospun cellulose nanofibers and their effect on the antimicrobial activity. Polymers for Advanced Technologies, 2018, 29(1): 394–400
25. Vahidi M, Tavasoli A, Rashidi A M. Preparation of amine functionalized UiO-66, mixing with aqueous N-methyldiethanolamine and application on CO_2 solubility. Journal of Natural Gas Science and Engineering, 2016, 28: 651–659
26. Hasan Z, Khan N A, Jhung S H. Adsorptive removal of diclofenac sodium from water with Zr-based metal-organic frameworks. Chemical Engineering Journal, 2016, 284: 1406–1413
27. Hashem T, Ibrahim A H, Woll C, Alkordi M H. Grafting zirconium-based metal-organic framework UiO-66-NH_2 nanoparticles on cellulose fibers for the removal of Cr(VI) ions and methyl orange from water. ACS Applied Nano Materials, 2019, 2(9): 5804–5808
28. Peterson G W, Lu A X, Epps T H III. Tuning the morphology and activity of electrospun polystyrene/UiO-66-NH_2 metal-organic framework composites to enhance chemical warfare agent removal. ACS Applied Materials & Interfaces, 2017, 9(37): 32248–32254
29. Wang J L, Guo X. Adsorption kinetic models: physical meanings, applications, and solving methods. Journal of Hazardous Materials, 2020, 390: 122156
30. Zaboon S, Abid H R, Yao Z X, Gubner R, Wang S B, Barifcani A. Removal of monoethylene glycol from wastewater by using Zr-metal organic frameworks. Journal of Colloid and Interface Science, 2018, 523: 75–85
31. Guo X, Wang J L. A general kinetic model for adsorption: theoretical analysis and modeling. Journal of Molecular Liquids, 2019, 288: 111100
32. Wang J L, Guo X. Adsorption isotherm models: classification, physical meaning, application and solving method. Chemosphere, 2020, 258: 127279
33. Mohammadi N, Khani H, Gupta V K, Amereh E, Agarwal S. Adsorption process of methyl orange dye onto mesoporous carbon material-kinetic and thermodynamic studies. Journal of Colloid and Interface Science, 2011, 362(2): 457–462
34. Lin S, Zhao Y F, Yun Y S. Highly effective removal of nonsteroidal anti-inflammatory pharmaceuticals from water by Zr(IV)-based metal- organic framework: adsorption performance and mechanisms. ACS Applied Materials & Interfaces, 2018, 10(33): 28076–28085
35. Peng Y G, Huang H L, Zhang Y X, Kang C F, Chen S M, Song L, Liu D H, Zhong C L. A versatile MOF-based trap for heavy metal ion capture and dispersion. Nature Communications, 2018, 9(1): 187
36. Chen Q, He Q Q, Lv M M, Xu Y L, Yang H B, Liu X T, Wei F Y. Selective adsorption of cationic dyes by UiO-66-NH_2. Applied Surface Science, 2015, 327: 77–85
37. Yang D Q, Hennequin B, Sacher E. XPS demonstration of π-π interaction between benzyl mercaptan and multiwalled carbon nanotubes and their use in the adhesion of Pt nanoparticles. Chemistry of Materials, 2006, 18(21): 5033–5038
38. Ting H, Chi H Y, Lam C H, Chan K Y, Kang D Y. High-permeance metal-organic framework-based membrane adsorber for the removal of dye molecules in aqueous phase. Environmental Science Nano, 2017, 4(11): 2205–2214
39. Ahmed M A, Abdelbar N M, Mohamed A A. Molecular imprinted chitosan-TiO_2 nanocomposite for the selective removal of rose bengal from wastewater. International Journal of Biological Macromolecules, 2018, 107: 1046–1053
40. Naushad M, Alothman Z A, Awual M R, Alfadul S M, Ahamad T. Adsorption of rose bengal dye from aqueous solution by amberlite Ira-938 resin: kinetics, isotherms, and thermodynamic studies. Desalination and Water Treatment, 2016, 57(29): 13527–13533
41. Cai R, Du Y P, Peng S J, Bi H C, Zhang W Y, Yang D, Chen J, Lim T M, Zhang H, Cao Y C, Yan Q. Synthesis of porous, hollow metal MCO_3 (M = Mn, Co, Ca) microstructures and adsorption properties thereof. Chemistry, 2014, 20(2): 421–425
42. Wang M, Ma Y F, Sun Y, Hong S Y, Lee S K, Yoon B, Chen L, Ci L J, Nam J D, Chen X Y, Suhr J. Hierarchical porous chitosan sponges as robust and recyclable adsorbents for anionic dye adsorption. Scientific Reports, 2017, 7(1): 18054